Excitation Coefficient Determination for an Antenna Elevation Network Using Installed Performance Radiation Measurements

Bernd Gabler, Alicja Schreiber
Microwaves and Radar Institute, German Aerospace Center (DLR), 82234 Oberpfaffenhofen, Germany, bernd.gabler@dlr.de

***Abstract*—Phased array antennas are typically designed from a set of largely similar radiating elements that are fed by a beam forming network (BFN). The ambient structure thereby impacts the installed performance and needs to be considered in the excitation coefficients determination. However, obtaining reliable results with purely numerical tools for aerospace composite material structures is questionable without electromagnetic parameter investigation. This work describes a method based on individual far-field measurements of the radiating sub-arrays in a Compact Antenna Test Range (CATR). The full array pattern is synthesized by planar near - field (PNF) techniques. Thereby, the excitation coefficients are optimized to mitigate the actual structure influence without the need for additional electromagnetic material properties investigation. The procedure is exemplified with a linear polarized Ka-band phased array for an airborne synthetic aperture radar application. Individual on structure slotted waveguide antenna (SWA) element measurements, excitation coefficients determination and the synthesized radiation pattern are shown. In a proof of concept with structures that are assumed perfectly conductive, measurement-based processing results are compared with simulations.**

***Index Terms*—antenna measurements, phased arrays, beam forming, post-processing techniques, far-field, near-field.**

I. Introduction

Phased array antennas are comprised of a set of individual radiating elements that are arranged within a limited area. The key advantage is their radiation pattern with a significant gain that is shaped and steered into a certain direction by adjusting the phase difference of the excitation coefficients in the beam forming network (BFN). Planar phased array antennas appear with a mechanically flat surface. In conjunction with having the electromagnetic propagation direction not necessarily orthogonal to the array aperture, their application for aerospace or military radar systems is advantageous. Besides that, new beam functionalities are required for planar antennas of the nowadays growing commercial markets. Structures, panels and lids from state-of-the-art materials are often not perfectly conductive. Thus, their electromagnetic properties are needed in simulation software to optimize the radiation pattern. Manufacturers do not always disclose the parameters and experimental determination for nonhomogeneous layered or fiber reinforced structures is challenging. The modular nature of phased array antennas counts for both, the radiating elements and the BFN that can even be separate for azimuth and elevation direction. In slotted waveguide antenna (SWA) arrays, the weighting function along the radiating elements is predefined by the waveguide feeding topology. The BFN complexity is therefore often reduced to only providing excitation coefficients for the orthogonal direction. Alternative to elaborate material property determination and simulation, row by row installed performance measurements of the SWA array are carried out to evaluate the BFN design parameters. Thereby, the excitation coefficients can be optimized in a virtual orthogonal network for the prediction of the full antenna performance prior to fabrication of the real network. In general, this method achieves good results for phased arrays with at least medium gain and sufficient inter element isolation.

A Ka - band SWA for an airborne synthetic aperture radar (SAR) application is developed at the Microwaves and Radar Institute of the German Aerospace Center (DLR), for enhancing the F-SAR system capabilities [1]. The entire Ka - band antenna system consists of a polarimetric interferometer with two transmit and up to four receive arrays. Each of them is mechanically tilted 40° off nadir and mounted on an aluminum structure backed carbon honeycomb panel. This assembly and a glass fiber reinforced windshield will be mounted on the bottom of the aircraft fuselage. In a first study, only the linear horizontal polarized array elements are developed. Section II explains design details of the SWA array and the beamforming network. Subsequently, the spherical measurements of SWA array rows in the DLR Compact Test Range, a dual reflector CATR, are described. Section III explains the processing steps to transform the far-field patterns by expanding the spherical wave into the near-field in a XY-plane. The individual near-field contributions are mathematically combined with applying individual complex weighting functions to synthesize the full array. Transforming the result to far-field with a planar near-field software module provides quasi real-time evidence on selecting optimum excitation coefficients. The method is validated by comparing measurements on a metal ground plane with full array simulations on a perfect electric conducting (PEC) surface.

II. SWA Array Design and Measurement

A. Ka-band SWA Prototype Design

The presented method is demonstrated on the antenna prototype of a slotted waveguide antenna (SWA), which operates at a center frequency of $f_0 = 35.5\,GHz$. The final antenna is specified to generate both vertically and horizontally linear polarized electromagnetic waves. To fulfill this requirement, two separate single antenna elements, each radiating in one polarization, are developed and arranged alternately to each other to build an antenna array. For the horizontally polarized antenna used in this work, a waveguide reduced in width and with transverse slots cut in the narrow wall is used. This configuration provides lower cross - polarization level compared to the setup with slant slots often described in the literature [2]. However, since in such case the current flow is not interrupted, which is a precondition for slot radiation using this technology, an additional structure is added inside the waveguide to perform this process. Here, a pair of shaped irises is used that is alternately placed on both sides of every slot to ensure in-phase output signals. Since the antenna array needs to have a shaped beam in both planes, amplitude distribution over the elements is required. Thus, in the azimuth direction (Phi 0° cut) the single antenna element consists of 22 slots and a cosine - taper is applied in order to get both, low sidelobe level as well as the desired half-power beam width. To ensure a stable radiation pattern over the frequency range, the single antenna element is fed centrally with a uniform H-plane T- junction.

In the elevation plane (Phi 90° cut) on the other hand, the antenna array consists of 4 single SWA elements, which are necessary to achieve the specified properties. As displayed in Fig. 1, the antenna elements generating vertical polarization are replaced with dummies in order to achieve a realistic environment for the horizontal polarized antenna. From the simulation made with the 22x4 prototype array, the power ratio between four elements was set in such a way that a low sidelobe level and desired half-power beam width is also obtained in this plane. In order to achieve this beamforming network, the outer elements have to get about 7.5 dB less power than the middle ones. The power ratio is realized by means of a uniform T-junction and a suitable directional coupler.

B. Measurements in the CATR

Fig. 1 depicts the validation measurement setup with the Ka-band 22x4 prototype array on the positioner of the DLR Compact Test Range. The SWA array is supported by a circular metal plate of 500 mm with absorber covered edges to adapt to the radiation boundary airbox conditions of the simulation. The spherical radiation patterns of all four SWA rows are measured in a sequence with the remaining elements terminated. Measurement frequency is swept over full Ka- band (28 GHz to 40 GHz) resulting in a downrange cellsize of 25 mm for the time gating in post-processing.

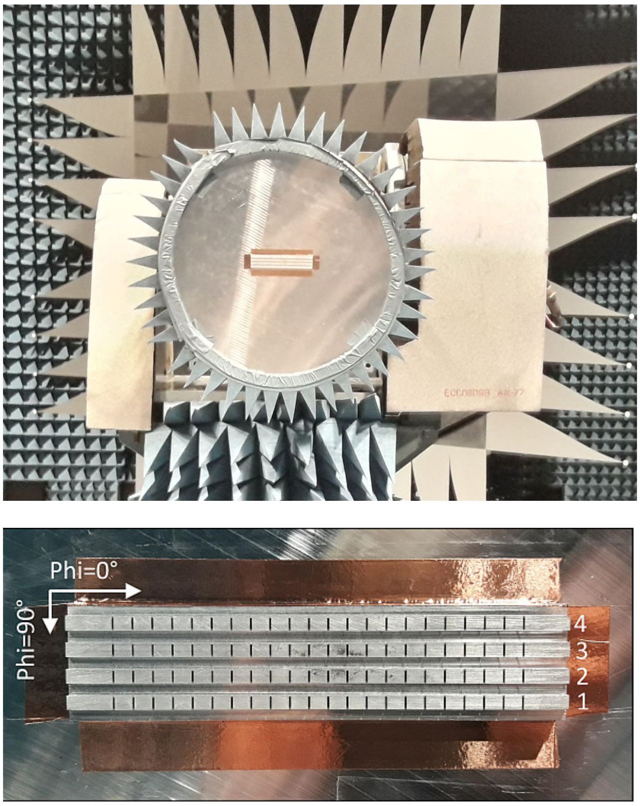

Fig. 1. Ka-band 22x4 array in the CATR (top), detail (bottom).

Partial realized gain at the reference port is obtained by applying the gain transfer method, pattern integration is used to calculate the directivity. Subsequently to a successful proof of concept, the quasi PEC backing surface will be replaced by the final airborne carbon honeycomb structure with unknown electrical parameters using a similar measurement setup.

III. Full Array Synthesis

The electrical field vector in the near-field of each individual sub-array is calculated by expansion of the spherical wave modes [3] from the far-field measurements. According to a planar near-field scanning implementation, a plane in XY direction at a virtual probe distance Z is sampled [4]. In a preparatory step, mathematical translation of the far-field measurement coordinate system to the probe is performed by differential phase shift. The plot in Fig. 2 illustrates the far-field principal cut radiation patterns of the four individual SWAs. Phi 90° cuts are complemented by Phi 0° cuts, respectively in lighter colors. Due to the flat installation of the AUT on the metal plate, the maxima are already in the direction of the probe. No further alignment step is necessary for a planar near-field scanner that captures at maximum the forward hemisphere [5]. In different configurations, with the radiating elements on tilted plates, extra alignment is advantageous for minimizing the uncertainties in the relevant main beam direction.

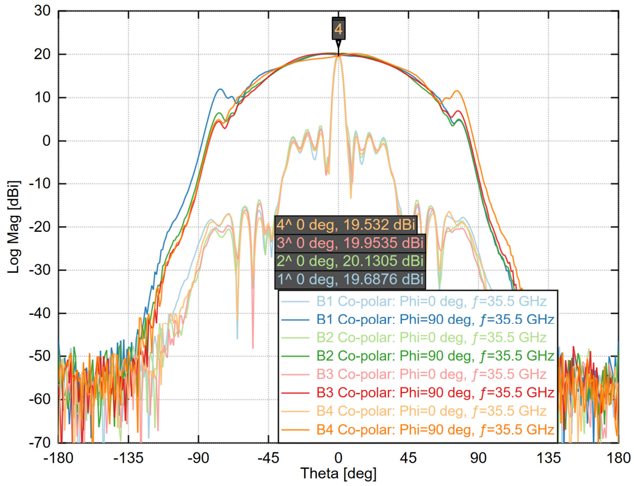

Fig. 2. Individual 4 SWA rows far-field directivity cuts Phi 0°, Phi 90°.

An adequate Euler rotation is optionally applied to the far-field in a Ludwig II polarization basis for alignment. Finally, the calculated individual SWA near-field contributions are superimposed. Instead of a simple vector addition, a complex weighting function is applied that corresponds to the excitation coefficients in the beam forming network. A last computation step is transforming the resulting near-field to spherical far-field [6].

A. Theoretical Background

A direct expansion of the base vectors is applied to transform from spherical modes to a planar field [3]:

$$\vec{E}(\theta,\varphi,\mathrm{r}) = \frac{\mathrm{k}}{\sqrt{\zeta}}\sum_{s=1}^{2}\sum_{n=1}^{\infty}\sum_{m=1}^{\infty} T_{smn}\vec{F}_{smn}^{(4)}(\theta,\varphi,\mathrm{r}), \quad (1)$$

where k denotes the wave number and ζ is the free space impedance. By using the method described in [3], the spherical wave coefficients T are derived from the far-field, with $\vec{F}_{smn}^{(4)}$ the spherical basis functions:

$$\begin{aligned}
\vec{F}_{1mn}^{(4)}(\theta,\varphi,\mathrm{r}) &= -\frac{1}{\sqrt{2\pi}}\frac{1}{\sqrt{n(n+1)}}\left(-\frac{m}{|m|}\right)^{n} h_n^{(2)}(kr)e^{-jm\varphi} \\
&\quad \left\{\frac{jm}{\sin\theta}\overline{P}_n^{|m|}(\cos\theta)\vec{e}_\theta + \frac{d}{d\theta}\left(\overline{P}_n^{|m|}(\cos\theta)\right)\vec{e}_\varphi\right\} \\
\vec{F}_{2mn}^{(4)}(\theta,\varphi,\mathrm{r}) &= \frac{1}{\sqrt{2\pi}}\frac{1}{\sqrt{n(n+1)}}\left(-\frac{m}{|m|}\right)^{n} e^{-jm\varphi} \\
&\quad \left\{h_n^{(2)}(kr)\frac{n(n+1)}{kr}\overline{P}_n^{|m|}(\cos\theta)\,\vec{e}_r\right. \\
&\quad +\frac{1}{kr}\frac{d}{d(kr)}\left(krh_n^{(2)}(kr)\right) \\
&\quad \left.\left[\frac{d}{d\theta}\left(\overline{P}_n^{|m|}(\cos\theta)\right)\vec{e}_\theta + \frac{jm}{\sin\theta}\left(\overline{P}_n^{|m|}(\cos\theta)\right)\vec{e}_\varphi\right]\right\}
\end{aligned} \quad (2)$$

In (2) $\overline{P}_n^{|m|}$ stands for the Normalized Associated Legendre functions and $h_n^{(2)}$ are the Hankel functions of the second kind. In contrast to a Fourier based expansion that is applied in the far-field, a direct use of (2) is more laborious. To accelerate the processing, precomputation and vectorization outlined in [7] are used. Furthermore, the calculation of multiple points is by nature parallel. Another constraint comes from the imaginary part of the Hankel function $h_n^{(2)}$, which is infinite at the origin. This is not a concern for spherical near-field applications where the modal expansion (1) is invalid for $n<kr$. In contrast, a very short distance z is prohibited in this application. As interim fix the imaginary part of $h_n^{(2)}$is set to zero for the case n<kr

As indicated in (1) Theta-Phi is for coordinate system as well as polarization base. The analyzed points are required in a Ludwig I definition which needs applying pre- as well as post-conversion [3][9]. The necessary origin translation in the (x,y,z)-direction is more convenient in the far-field using

$$\begin{aligned}
&\vec{E}(\Delta_x,\Delta_y,\Delta_z,\theta,\varphi) = \\
&\vec{E}(\theta,\varphi)e^{j(\Delta_x\sin\theta\cos\varphi+\Delta_y\sin\theta\sin\varphi+\Delta_z\cos\theta)},
\end{aligned} \quad (3)$$

with $\Delta_{\{x,y,z\}}$ the required offset shift. Two methods are available for a rotation of the far-field: resampling in the angular domain or using the rotation operator to the spherical modes [3]. The near-field contributions of each radiating element are shifted by a certain amplitude and gain that is representing the virtual excitation network.

The resulting planar near-field data are transformed to the angular spectrum $\vec{F}_T$ using [6]

$$\vec{F}_T(k_x,k_y) = \iint\left(E_x\vec{e}_x + E_y\vec{e}_y\right)e^{j(k_xx+k_yy)}\,dx\,dy. \quad (4)$$

Similar to standard planar near-field measurements, only x and y Ludwig-I components are considered. In this application, the absence of a physical probe requires no probe correction. The far-field tangential components are calculated with

$$\vec{E}_{ff}(k_x,k_y) = j\frac{\sqrt{1-k_x^2-k_y^2}}{\lambda}\vec{F_T}(k_x,k_y). \quad (5)$$

It can be seen in (5) that k_x and k_y are inside the unit circle, consequently this is a projection to the forward hemisphere. Therefore, allowing transformations to other polarizations or coordinate system. Subsequently, a directivity calibration of the antenna pattern can be realized by integration of the far-field pattern $\vec{E}_{ff}$ in (5) over the unit circle.

B. Synthesis of the Full Array in a Proof of Concept

The color-coded contour plot of Fig. 3 with the center section near-field plane in E_x was computed from measurements of the horizontally polarized SWA row 4. It clearly shows the field distribution in X-direction along the radiating waveguide structure and the reflections on the neighboring metal plate to top of the plot. The resulting synthesized near-field is computed with applying excitation coefficients that represent an elevation BFN with a coupler. In Fig. 4 both far-out SWAs are exemplary attenuated by 7.5 dB with respect to the center rows. ARCS Analysis [8] is used for the entire measurement data processing.

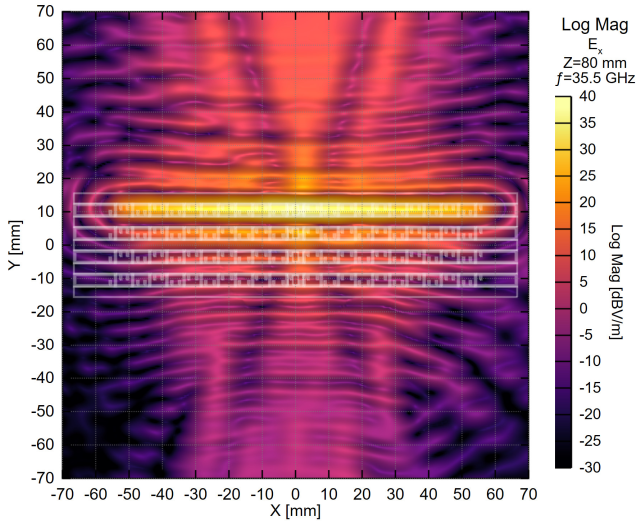

Fig. 3. Near-field E_x magnitude of SWA row 4 at a virtual probe distance of Z=80 mm, array outline overlay in white.

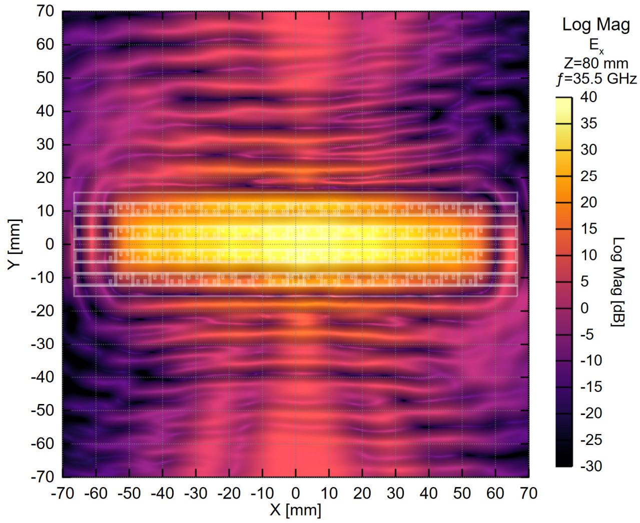

Fig. 4. Near-field E_x magnitude of a synthesized full array from 4 SWA rows with a virtual BFN, probe distance Z=80 mm, array outline overlay in white.

IV. Validation of the Synthesized Pattern

A selection of two different excitation coefficients representing virtual elevation BFNs are applied for synthesizing the array near-field, which is subsequently transformed to far-field with a PNF processing module. Reference patterns from both, array measurements with a corresponding machined hardware BFN and pure simulation, are compared with the results. For comparability, magnitudes refer to directivity, in order to bypass the losses in the hardware BFM of the SWA array measurements. To highlight the influence of the boundary conditions, the simulation results in Fig. 5 and Fig. 6 (blue) refer to an infinite PEC ground plane.

A. Result for an elevation BFN with uniform distribution

For the airborne SAR application, an elevation BFN with uniform distribution is practically useless due to the high sidelobe levels. However, for its simplicity, this design is ideally suited for a proof of concept. Results with principal cuts of this setup are depicted in Fig. 5. TABLE I. summarizes the parameters of the simulated, the measured and the synthetic array uniform BFM. The results show a high degree of similarity for the maxima of the directivity patterns and half-power beamwidth. The difference in sidelobe levels illustrates the sensitivity of the setup to small phase variations at a free space wavelength of 8.45 mm at the center frequency.

B. Result for an elevation BFN with a coupler

A coupler, referred to as "coupler 7.5", is feeding the center rows of the array with equal amplitudes and phase, while the far-out rows are respectively attenuated by 7.5 dB. The plot with the cuts in Fig. 6 and the parameters in TABLE II. confirms that sidelobe levels are substantially lower. The corresponding antenna array parameters are listed in TABLE II. All main lobe parameters agree well. However, sidelobe levels are sensitivity to phase differences in the BFN. In comparison to the hardware BFN version, the synthesized array reconstructs the pattern remarkably well within almost the full hemisphere.

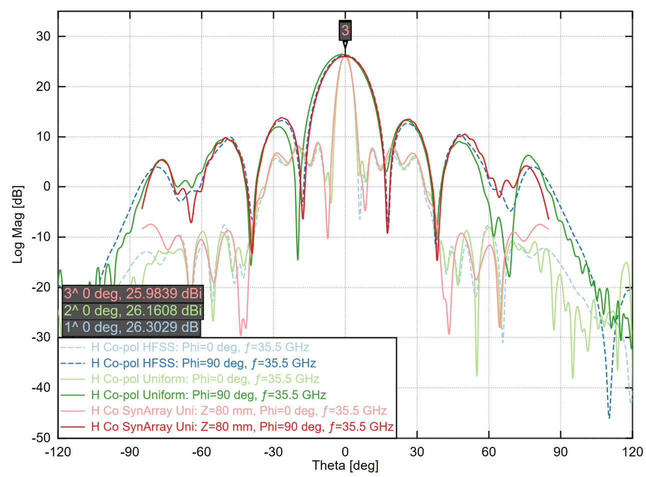

Fig. 5. Uniform distribution BFN, simulation (blue), measurement (green), synthetic array (red), directivity cuts Phi 0°, Phi 90°.

TABLE I. UNIFORM BFM

Parameter Phi 90°	*Simulated uniform BFM*	*Measured uniform BFM*	*Synthetic array uniform BFM*
Maximum directivity	26.30 dBi	26.16 dBi	25.98 dBi
Half-power beamwidth	15.68°	15.99°	15.90°
SLL 1 -	-13.06 dBn	-14.45 dBn	-12.18 dBn
SLL 1 +	-13.59 dBn	-13.17 dBn	-12.49 dBn

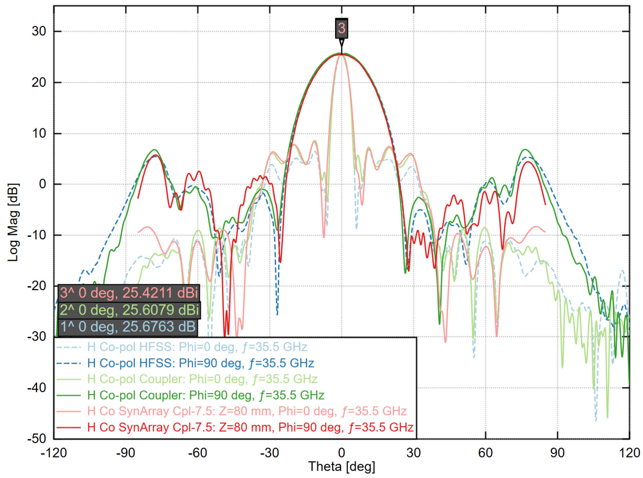

Fig. 6. Coupler 7.5 BFN, simulation (blue), measurement (green), synthetic array (red), directivity cuts Phi 0°, Phi 90°.

TABLE II. COUPLER 7.5 BFN

Parameter Phi 90°	***Simulated coupler 7.5 BFM***	***Measured coupler 7.5 BFM***	***Synthetic array coupler 7.5 BFM***
Maximum directivity	25.68 dBi	25.61 dBi	25.42 dBi
Half power beamwidth	19.32°	19.58°	19.34°
SLL 1 -	-27.43 dBn	-26.66 dBn	-23.99 dBn
SLL 1 +	-30.69 dBn	-28.31 dBn	-35.64 dBn

V. CONCLUSION

The proof of concept demonstrates that the full array pattern can be synthesized from sub-array measurements with spherical and planar techniques. The beam is precisely shaped with fine phase and amplitude adjustments in the virtual BNF to reach a high agreement to both simulation results and full array measurements. In future applications on mixed material non-PEC surfaces, the method will be used for exact evaluation of the excitation coefficients prior to machining the BFN. The fact that the environmental structure electrical parameters are not needed for the simulation tool is beneficial to speed up the design process. Improvement opportunities for the synthetization are in an advanced planar transformation including E_z , and in overcoming the scanning restriction in z-direction by using current sources for computing the field inside the unit circle.

ACKNOWLEDGMENT

The authors sincerely thank L.G.T van de Coevering from March Microwave Systems B.V. for his valuable support in this work.

REFERENCES

[1] A. Schreiber, M. Limbach, B. Gabler and A. Reigber, “Horizontally Polarized Antenna Array for an Airborne Ka - PolInSAR System,” 16th European Conference on Antennas and Propagation (EuCAP), IEEE 2022, pp. 1-5, doi: 10.23919/EuCAP53622.2022.9769576.

[2] L. Josefsson, S.R. Rengarajan, Slotted Waveguide Array Antennas. London, U.K.: The Institution of Engineering and Technology, 2018.

[3] Hansen (ed), Spherical Near-Field Antenna Measurements. Peter Peregrinus Ltd. 1988.

[4] B. Gabler, D. Lorente and L. G. T. van de Coevering, "Synthesis of a Phased Array with Planar Near-Field Techniques Based on Far-Field Measurements of a Sub-Array in a CATR," 43rd Antenna Measurement Techniques Association Symposium (AMTA), 2021, pp. 1-5, doi: 10.23919/AMTA52830.2021.9620679.

[5] S. Gregson, J. McCormick, D. J. Van Rensburg, and C. Parini, Theory and Practice of Modern Antenna Range Measurements. London, U.K.: The Institution of Engineering and Technology, 2014.

[6] S. Gregson, J. McCormick, and C. Parini, Principles of Planar Near-Field Antenna Measurements.. London, U.K.: The Institution of Engineering and Technology, 2007.

[7] T. Limpanuparb, J. Milthorpe, “Associated Legendre Polynomials and Spherical Harmonics Computation for Chemistry Applications” Proceedings of The 40th Congress on Science and Technology of Thailand; 2014, https://arxiv.org/abs/1410.1748.

[8] ARCS Analysis Manual v1.77xs, Nuenen, the Netherlands, March Microwave Systems, March 2022.

[9] A.C. Ludwig, “The definition of Cross-polarization”, IEEE Trans. Antennas Propagation, vol. AP-21 no 1, pp. 116-9, Jan. 1973.